Coarse-grained reduced Mo Ti1–Nb2O7+ anodes for high-rate lithium-ion batteries

Coarse-grained Reduced $Mo_xTi_{1-x}Nb_2O_{7+y}$ Anodes for High-Rate Lithium-ion Batteries

Lijiang Zhao [a], Shitong Wang [b], Yanhao Dong [b,*], Wei Quan [e], Fei Han [b], Yimeng Huang [c], Yutong Li [d], Xinghua Liu [a], Mingda Li [b], Zhongtai Zhang [d], Junying Zhang [a,**], Zilong Tang [d,***], and Ju Li [b, c,*]

[a] Key Laboratory of Micro-nano Measurement, Manipulation and Physics (Ministry of Education), School of Physics, Beihang University, Beijing 100191, China.

[b] Department of Nuclear Science and Engineering, Massachusetts Institute of Technology, Cambridge, Massachusetts 02139, USA

[c] Department of Materials Science and Engineering, Massachusetts Institute of Technology, Cambridge, Massachusetts 02139, USA

[d] State Key Lab of New Ceramics and Fine Processing, School of Materials Science and Engineering, Tsinghua University, Beijing 100084, China

[e] China Automotive Battery Research Institute Co., Ltd., Beijing 101407, China

General Research Institute for Nonferrous Metals, Beijing 100088, China

***** Corresponding author.

****** Corresponding author.

******* Corresponding author.

E-mail addresses: zjy@buaa.edu.cn (Junying Zhang), tzl@tsinghua.edu.cn (Zilong Tang), dongyh@mit.edu (Yanhao Dong) , liju@mit.edu (Ju Li)

Abstract:

High-volumetric-energy-density lithium-ion batteries require anode material with a suitable redox potential, a small surface area, and facile kinetics at both single-particle and electrode level. Here a family of coarse-grained molybdenum substituted titanium niobium oxides $Mo_xTi_{1-x}Nb_2O_{7+y}$ (single crystals with 1~2 μm size) underwent hydrogen reduction treatment to improve electronic conduction, which is able to stably deliver a capacity of 158.5 mAh g^{-1} at 6,000 mA g^{-1} (65.2 % retention with respect to its capacity at 100 mA g^{-1}) and 175 mAh g^{-1} (73 % capacity retention over 500 cycles) at 2,000 mA g^{-1}, respectively. Via careful *in situ* electrochemical characterizations, we identified the kinetic bottleneck that limits their high-rate applications to be mainly ohmic loss at the electrode level (which mostly concerns electron transport in the composite electrodes) rather than non-ohmic loss (which mostly concerns Li^+ lattice diffusion within individual particles). Such a kinetic problem was efficiently relieved by simple treatments of Mo substitution and gas-phase reduction, which enable full cells with high electrode density, and high volumetric energy/power densities. Our work highlights the importance of diagnosis, so that modifications could be made specifically to improve full-cell performance.

Keywords: Titanium niobium oxides; Molybdenum substitution; Hydrogen reduction; Kinetics; Lithium-ion batteries

1. Introduction

Advanced lithium-ion batteries (LIBs) are under rapid development to address the ever-increasing demand of higher energy and power densities, longer cycling life, and better safety in a variety of applications, including portable electronics, electric vehicles, and large-scale energy storage systems [1]. For high-rate LIBs that can be fast-charged and are able to deliver large discharge current/power, many cathode materials are available, including nano lithium iron phosphate $LiFePO_4$, as well as coarse-grained materials of spinel $LiNi_{0.5}Mn_{1.5}O_4$ and layered $LiNi_{1-x-y}Co_xMn_yO_2$. On the anode side, commercial graphite is not suitable for high-rate applications because its redox potential is too close to lithium metal (0 V vs. Li^+/Li) and is prone to dendrite formation under high charging rates. A good anode candidate is nano lithium titanate $Li_4Ti_5O_{12}$, which has a suitable redox potential (~1.55 V vs. Li^+/Li), fast kinetics, and good cycling stability [2-11]. However, nano $Li_4Ti_5O_{12}$ has a low packing density and thus a low volumetric energy density, while coarse-grained $Li_4Ti_5O_{12}$ with higher packing density suffers from poor kinetics [12]. Therefore, it is a great challenge to find a suitable coarse-grained anode with a suitable redox potential for high-rate high-(volumetric)-energy-density LIBs.

Previous efforts to address this issue lead to the development of Nb-based materials including intermediate-temperature-phase niobium oxides (T-Nb_2O_5 and TT-Nb_2O_5) [13, 14], titanium niobium oxides (e.g., $TiNb_2O_7$ and $Ti_2Nb_{10}O_{29}$) [15-17] and tungsten niobium oxides (e.g., $W_5Nb_{16}O_{55}$ and $W_{16}Nb_{18}O_{93}$) [18], which mainly rely on Nb^{5+}/Nb^{3+} double-electron redox with equilibrium potential of around 1.6 V vs. Li^+/Li and have high lithium-ion diffusivity in the active-material lattice that enables micron-size powders to be used as high-rate anodes. Among such Nb-based candidates, $TiNb_2O_7$ is of particular interest, which has attracted continuous attention in both academia and the battery industry since its first report as LIB anode in 2011 [16, 19-29]. Many attempts have been made to further improve its high-rate performance (e.g., modifications in the morphology, doping [30-34], coating [28] and synthesis of hybrid composites [35-37]), among which nano-structuring that shortens diffusion distance is probably the most popular method to enhance the kinetics [23-25, 29, 38-43]. However, such nanomaterials often suffer from two types of problems. First, nanomaterials typically have large specific surface area, which exposes a large number of fresh surfaces to the electrolyte and activates side reactions. This would irreversibly consume the precious lithium inventory and liquid electrolyte in practical full cells, lower the coulombic efficiency (CE), and lead to poor cycling stability and other problems such as gassing. Second, nanomaterials can easily get jammed during electrode preparation and calendaring, which lowers the packing density and full-cell volumetric energy density. Therefore, it is important to develop high-performance coarse-grained $TiNb_2O_7$, which requires mechanistic understandings of the rate-limiting factors under high rates and solves the kinetic problems accordingly.

In this work, a series of molybdenum substituted (substituting Ti in $TiNb_2O_7$) titanium niobium oxides $Mo_xTi_{1-x}Nb_2O_{7+y}$ was systematically investigated, aiming to clarify the rate-limiting factors for their high-rate applications and to improve the electrochemical performance accordingly. We found under high-rate conditions, the cells were kinetically limited by huge impedance, mainly from ohmic loss that mostly concerns electron transport in the composite electrodes (consisting of active material, conductive carbon, binder, and porosity soaked with liquid electrolytes) rather than non-ohmic loss that mostly concerns Li^+ diffusion within individual particles. It is further supported by the measured lithium ion diffusivity on the order of 10^{-10} cm^2 s^{-1} (similar to that in high-voltage spinel $LiNi_{0.5}Mn_{1.5}O_4$, a known cathode for high-rate applications, and much higher than that in $LiFePO_4$ and $Li_4Ti_5O_{12}$) [4, 44], which in principle should allow 1 μm particles to be cycled under 36 C rate without any diffusive bottlenecks. Correspondingly, we demonstrated Mo substitution and atmospheric reduction are simple and effective methods to reduce the cell impedance and boost high-rate performance, which allows coarse-grained $Mo_{0.25}Ti_{0.75}Nb_2O_{7.25-y}$ to stably deliver ~158 mAh g^{-1} at a current density of 6,000 mA g^{-1} and with longer-term durability (≈73 % capacity retention over 500

cycles at 2,000 mA g^{-1}) over the voltage window of 1.0~1.5 V vs. Li^+/Li. When paired with $LiNi_{0.5}Mn_{1.5}O_4$ cathodes in full cells, high volumetric energy (1338 Wh L^{-1}) and power density (31200 W L^{-1}) have been achieved with high electrode density.

2. Experimental

2.1 Material synthesis

$TiNb_2O_7$ (TNO), $Mo_{0.125}Ti_{0.875}Nb_2O_{7.125}$, $Mo_{0.25}Ti_{0.75}Nb_2O_{7.25}$ (MTNO), and $Mo_{0.5}Ti_{0.5}Nb_2O_{7.5}$ were synthesized by mixing Nb_2O_5 (99.99 % purity), MoO_3 (99.998 % purity) and TiO_2 (99.8 % purity) using high-energy ball mill, followed by high-temperature treatment at 1125 ^oC for 5 h with a heating rate of 2 ^oC min^{-1} and natural cooling. To synthesize R-MTNO and R-TNO, MTNO and TNO powders were treated in flowing H_2 (5 %, balanced with Ar; flow rate 50 sccm) at 600 ^oC for 6 h with a heating rate of 2 ^oC min^{-1} and natural cooling.

2.2 Materials characterizations

Scanning electron microscope (SEM, MERLIN VP Compact) and high-resolution TEM (HRTEM, Talos 200X, Thermo Fisher Scientific, US) were used to characterize the morphology and the structures. X-ray diffraction (XRD, Rigaku D/Max-B X; Cu Kα radiation λ= 1.5418 Å) was used to characterize the phase. X-ray photoelectron spectrometer (XPS, VG microtech ESCA2000) was used to characterize the surface chemistry. Inductively coupled plasma mass spectroscopy (ICP-MS, iCP QC, Thermo Fisher Scientific, US) measurements were conducted to analyze the compositions. The specific surface area was measured by Autosorb-iQ2-MP (Quanta Chrome) and calculated following the standard Brunauer-Emmett-Teller (BET) method.

2.3 Electrochemical characterizations

Preparation of half cells: To prepare the composite working electrodes, active materials, conductive carbon (Super P), sodium carboxymethyl cellulose (CMC) and polymerized styrene butadiene rubber (SBR) were mixed with a weight ratio of 90:5:2.5:2.5 to form a homogeneous slurry, spread on commercial Al foils, and dried at 110 ^oC in vacuum for 12 h. The mass loading of active materials (1~2 mg cm^{-2}) was controlled by adjusting the gap of the scraper. 1 M $LiPF_6$ dissolved in ethylene carbonate (EC), dimethyl carbonate (DMC) and ethyl methyl carbonate (EMC) in a 1:1:1 volume ratio was used as the electrolyte. Microporous polypropylene films (Celgard 2500) was used as the separators. Cell assembly (CR2032 type) was carried out in an Ar glove box with oxygen and water contents below 1.0 ppm and 0.5 ppm, respectively. Charge/discharge tests were conducted between 1.0 and 2.5 V vs. Li^+/Li at varied current densities using LAND battery testing system (CT-2001A). For the cycling performances, each battery was pre-activated for 3 cycles at 100 mA g^{-1}. Galvanostatic

intermittent titration technique (GITT) measurements were conducted using LAND battery testing system (CT-2001A) with two different settings: (1) with a titration current of 4000 mA g^{-1} and a titration time of 30 s, followed by 15 h relaxation, or (2) a titration current of 50 mA g^{-1} and a titration time of 1 h, followed by 15 h relaxation.

Preparation of full cells: $LiNi_{0.5}M_{1.5}O_4$//R-MTNO coin-cell type full cells (CR2032 type) were assembled. The cathodes were prepared similarly with a weight ratio of 85:7.5:7.5 for active material ($LiNi_{0.5}Mn_{1.5}O_4$): conductive carbon (Super P): polyvinylidene fluoride (PVDF, 7.5 wt %). The optimized cathode/anode areal capacity was set as 1.13:1, with the mass loading of active materials for cathodes and anodes around 18 mg cm^{-2} and 8 mg cm^{-2}, respectively. For $LiNi_{0.5}M_{1.5}O_4$ half cells and $LiNi_{0.5}M_{1.5}O_4$//R-MTNO full cells, a constant-voltage charging step was applied at the upper cut-off voltage until the current reaches 1/10 of the one used in the constant-current charging step.

3. Results and discussion

We started by exploring the compositional space of $Mo_xTi_{1-x}Nb_2O_{7+x}$. A series of samples $TiNb_2O_7$ (x=0, abbreviated as TNO hereafter), $Mo_{0.125}Ti_{0.875}Nb_2O_{7.125}$ (x=0.125), $Mo_{0.25}Ti_{0.75}Nb_2O_{7.25}$ (x=0.25, abbreviated as MTNO hereafter), and $Mo_{0.5}Ti_{0.5}Nb_2O_{7.5}$ (x=0.5) were prepared by mixing raw materials of Nb_2O_5, TiO_2 and MoO_3 with the targeted stoichiometry (the obtained stoichiometries were confirmed by ICP-MS measurements in Table S1), followed by high-temperature solid-state synthesis at 1125 ^oC for 5 h in air. Here we assumed transition metals all take the highest valence, i.e., Ti^{4+}, Nb^{5+} and Mo^{6+}, to calculate the oxygen stoichiometry. Indeed, all the powders have similar light-yellow color (insets of Fig. 1a~d), which suggests minimal mid-gap states and supports the argument that Ti, Nb, and Mo all take their highest valences with d^0 electronic configurations. As shown by the scanning electron microscopy (SEM) images in Fig. 1a~d, all samples have coarse-grained microstructures with average particle sizes of around 1~2 μm. Meanwhile, the substitution of Ti by Mo slightly promotes the growth of the particles and changes the equiaxial morphologies in Fig. 1a~b to elongated plate-like shapes in Fig. 1c~d. For the crystal structure, the X-ray diffraction (XRD) patterns as well as Rietveld refinement analysis suggest Mo substitution has a minimal effect and all four materials follow the same structure as $TiNb_2O_7$ (JCPDF 39-1407, Fig. S1 and Table S2). This is an interesting observation considering the extra oxygen content introduced by Mo^{6+} substitution (of Ti^{4+}) to balance the charge, yet the crystal structure is robust enough to accommodate such changes. It can be understood from the so-called "crystallographic shear structures", where the formation of crystallographic shear planes is preferred over the formation of oxygen vacancies upon reduction and *vice versa* [45, 46]. More

specifically, in the referred structure of $TiNb_2O_7$ (crystal structure shown in Fig. S2), the cations sit in five different octahedral sites, marked as *M*1 to *M*5 in the right panel of Fig. S2 (detailed structural information listed in Table S3), and these octahedra are either corner- or edge-connected. Among them, *M*1 has 6 corner-shared octahedral neighbors, *M*2 has 2 edge-shared (with *M*2) and 3 corner-shared neighbors, *M*3 has 2 edge-shared (with *M*4 and *M*5) and 3 corner-shared neighbors, *M*4 has 2 edge-shared (with *M*3 and *M*5) and 3 corner-shared neighbors, and *M*5 has 4 edge-shared (with 2×*M*3 and 2×*M*4) and 2 corner-shared neighbors. According to Pauling's rule of polyhedron packing, higher-valence cations are less favorable to occupy face-/edge-shared anion polyhedral due to strong Coulomb repulsion. Therefore, the occupancy of Nb^{5+} follows the rank of *M*1>*M*2≈*M*3≈*M*4>*M*5 in $TiNb_2O_7$ (as supported by occupancy data in Table S3), which should also apply to Mo^{6+} in $Mo_xTi_{1-x}Nb_2O_{7+x}$. As a result, the extra oxygen brought in by the substitutional Mo^{6+} doping could be accommodated by de-coordinating the "dense" edge-sharing polyhedra to more flexible corner-sharing ones, instead of forming high-energy interstitial oxygen defects. However, its influence on the XRD pattern is rather small, which impedes more detailed analysis at the present stage and may be worthwhile for future studies.

Next, their electrochemical performances were investigated in half cells using Li metal as the counter and reference electrode. At small charge/discharge current density of 100 mA g^{-1}, the four compositions show similar redox behaviors (Fig. S3a), whereas Mo substitution slightly increases the capacity from 236.6 mAh g^{-1} for TNO to a peak value of 251.8 mAh g^{-1} for MTNO. At larger charge/discharge current densities up to 6,000 mA g^{-1} (Fig. 1e, Fig. S3b~c, and Fig. S4~5), MTNO also showed the best retention, offering impressive high-rate capacity of 196.1 mAh g^{-1} (77.0 % retention with respect to its capacity at 100 mA g^{-1}) at 1,000 mA g^{-1} (~5 C; C rate estimated from actual charge/discharge time) and 141.2 mAh g^{-1} (55.4 % retention with respect to its capacity at 100 mA g^{-1}) at 6,000 mA g^{-1} (~40 C). Therefore, MTNO is selected as the optimal composition for further detailed investigations.

We next conducted gas-phase reduction to engineer the electronic conductivity of the samples. It is known that in many transition metal oxides, reduction treatment assisted by fuel gases (e.g., H_2 and CO), carbon, reactive metals (e.g., Al) and applied voltage is able to tune the oxygen stoichiometry, enhance polaron concentration, and trigger metal-insulator-transitions as well as phase transitions [47-49]. In our cases, we treated TNO and MTNO in 5% H_2 (balanced with 95% Ar) at 600 ^oC for 6 h to obtain reduced TNO ($TiNb_2O_{7-y}$, abbreviated as R-TNO) and reduced MTNO ($Mo_{0.25}Ti_{0.75}Nb_2O_{7.25-y}$, abbreviated as R-MTNO). As shown in the insets of Fig. 1f and g, it completely changed the yellowish colors of the untreated powders to black ones, indicating changes in light absorption caused by

reduction-generated mid-gap states [50, 51]. (From the XPS data in Fig.1 h,k, Mo^{6+} and Nb^{5+} ions were confirmed to be partially reduced after hydrogen reduction.) Such states are most likely electron polarons in reduced transition-metal oxides, which offers more electronic charge carriers in electrochemical applications. Interestingly, we again note minimal changes in the crystal structure with respect to the reference structure of $TiNb_2O_7$, as shown by XRD in Fig. S1e~f. This is consistent with the results discussed above and oxygen loss in R-TNO and R-MTNO is probably accommodated by the formation of more edge-shared polyhedra (lower valences of reduced transition-metal ions again facilitate such process), instead of creating oxygen vacancies. Nevertheless, lattice distortions can still be introduced upon oxygen loss, as confirmed by high-resolution TEM (HRTEM) in Fig. S6, and they could be beneficial to the lithium-ion or electron transport [52]. Regarding the microstructure, the obtained R-TNO and R-MTNO have similar coarse-grained morphology (Fig. 1f and g) to TNO and MTNO and similarly low specific surface areas of ~1 $m^2\ g^{-1}$ (see data from Brunauer-Emmett-Teller, BET, measurements in Table S4). X-ray photoelectron spectroscopy (XPS) measurements were then conducted to study the surface chemistry as an indication of the electron doping level. For Nb 3*d* spectra (Fig. 1h), Nb $3d_{5/2}$ & $3d_{3/2}$ peaks in reduced samples shift towards lower binding energy, from 206.9 eV & 209.6 eV in TNO and 206.8 eV & 209.5 eV in MTNO to 206.7 eV & 209.4 eV in R-TNO and 206.5 eV & 209.2 eV in R-MTNO, respectively. For Ti 2*p* and O 1*s* spectra of XPS (Fig. 1i~j), R-TNO and MTNO change little compared with the pristine sample of TNO, but R-MTNO exhibit a slight shift towards lower binding energy. It suggests in TNO structure, Ti^{4+} is more difficult to be reduced than Nb^{5+} [30]. For Mo 3*d* spectra (Fig. 1k), an obvious shift towards lower binding energy is identified in R-MTNO, suggesting a reduction of Mo^{6+} [53]. Therefore, the XPS data confirmed reduction of the oxides and electron doping in both H_2-treated samples, and R-MTNO is more reduced than R-TNO [54, 55], which is expected to facilitate electron transport during electrochemical cycling [50, 51]. Their electrochemical performances were then investigated in half cells using Li metal as the counter and reference electrode at charge/discharge current densities up from 100 mA g^{-1} to 6,000 mA g^{-1} (Fig. S3~4). As summarized in Fig. 2a~b, reduction treatment of TNO and MTNO maintains their capacity below 200 mA g^{-1} and increases their high-rate capacity up to 6,000 mA g^{-1}. Overall, R-MTNO offers the highest high-rate capacity of 208.0 mAh g^{-1} (83.8 % retention with respect to its capacity at 100 mA g^{-1}, obtained after 15 cycles within the same set of rate-capability tests) at 1,000 mA g^{-1} (~5 C) and 158.5 mAh g^{-1} (65.2 % retention with respect to its capacity at 100 mA g^{-1}, obtained after 30 cycles within the same set of rate-capability tests) at 6,000 mA g^{-1} (~40 C). Furthermore, R-MTNO has the highest first-cycle coulombic efficiency of 98.5 % among all the investigated materials (see summary in Table S4). Their cycling performances were investigated next (Fig. 2c), among which R-MTNO shows the best capacity retention of 73 % over 500 cycles at 2,000 mA g^{-1} (~12 C). R-

MTNO also demonstrates superior cycling stability for 300 cycles under 200 mA g^{-1} (from 245 to 223 mAh g^{-1}), and 1000 mA g^{-1} (from 194 to 184 mAh g^{-1}, with capacity decays of ~0.02 % per cycle). Even at a high current density of 4000 mA g^{-1}, the R-MTNO still shows very stable cycling with capacity decay of ~0.08 % per cycle (Fig. 2d). (Note that there shows a gradual capacity increase in early cycles (Fig. S7), which could be related to the activation process of the composite electrodes, including electrolyte wetting, charge transfer, and ion/electron percolation.) Therefore, Mo substitution and reduction treatment synergistically improve the high-rate performance of the investigated compounds.

Now that the experimental advantages are settled, we seek to understand the bottlenecks that limit the high-rate performance of the Nb-based anodes and how Mo substitution and hydrogen reduction treatment help. Galvanostatic intermittent titration technique (GITT) measurements were conducted on TNO, R-TNO, MTNO, and R-MTNO with a current density of 4,000 mA g^{-1} and a duration of 30 s for each titration step, followed by 15 h rest for each relaxation step. As shown in Fig. S8, their high-rate capacities are kinetically limited by huge overpotential developed under such non-equilibrium conditions. Even for the best sample R-MTNO (in terms of high-rate performance), the discharge voltage shoots below 1.0 V (vs. Li^+/Li) in the 8th titration step with a huge overpotential of 0.52 V, while the equilibrium voltage after the 8th relaxation step is as high as 1.44 V (vs. Li^+/Li). We further decoupled the overpotential into ohmic loss (which relaxes immediately after switching from the titration step to the relaxation step) and non-ohmic loss (which relaxes slowly after switching to the relaxation step) and compared them in Fig. 3a as a function of the discharge voltage. We found the ohmic loss in the range of 200~400 mV always dominates over the non-ohmic one for all the samples, which suggests electron transport in the composite electrodes (consisting of active material, conductive carbon, binder and pore soaked with liquid electrolytes) could be the rate-limiting factor for high-rate performance. To further verify that Li^+ diffusion through the lattice of individual oxide particles is not rate-limiting, we conducted GITT measurement at a small titration current density of 50 mA g^{-1} (Fig. S9) and calculated the lattice diffusivity of lithium D_{Li} according to: [56, 57]

$$D_{Li} = \frac{4}{\pi}\left(\frac{V_M}{AFZ}\right)^2\left[I_0\frac{dE/d\delta}{dE/d\sqrt{t}}\right]^2,\ t \ll \frac{L^2}{D_{Li}} \qquad (1)$$

where V_M is the molar volume of active material (for simplification, here we used 79.88 $cm^3\ mol^{-1}$ for $TiNb_2O_7$), A is the contact area between electrolyte and electrodes, F is the Faraday constant, I_0 is the applied titration current, Z is 1 (valence of lithium ion), E is electrode voltage, δ is the deviation from the initial stoichiometry, L is the thickness of the electrode, and t is the duration of the titration step. The calculated D_{Li} of all the four electrodes (Fig. 3b) is on the order of ~10^{-10} $cm^2\ s^{-1}$, which is similar

to that of high-voltage spinel $LiNi_{0.5}Mn_{1.5}O_4$, a known coarse-grained cathode for high-rate applications, and much higher than that of $LiFePO_4$ (10^{-15}~10^{-14} cm^2 s^{-1}) and $Li_4Ti_5O_{12}$ (10^{-19}~10^{-9} cm^2 s^{-1}) [4, 44]. Taking the average value of 10^{-10} cm^2 s^{-1}, an estimation from the random walk model diffusion length = (diffusivity × time)$^{1/2}$ would allow 1 μm particles to be cycled under 36 C rate without any lattice diffusion bottlenecks. It again suggests lattice diffusion of Li^+ and polarons within individual particles is not the rate-limiting factor for the high-rate applications. This observation of robust lattice diffusion of lithium for coarse-grained oxides under high rates is impressive and reminds us about the pseudocapacitive charge-storage behaviors observed in many nanomaterials for super-capacitor applications. Following the diagnosis method in the field of super-capacitors [58, 59], we separate the diffusion-controlled capacity (abbreviated as "diffusive" in Fig. 3d) and capacitive capacity (that is not diffusion-controlled; abbreviated as "capacitive" in Fig. 3d) according to:

$$Q = k_1 + k_2 (\Delta t)^{1/2} \qquad (2)$$

where Q is the specific discharge energy (calculated from Fig. S4), Δt is the discharge time, k_1 is a constant representing the rate-independent capacitive contribution to the specific energy, and k_2 is a constant setting $k_2(\Delta t)^{1/2}$ as the rate-dependent diffusion-controlled contribution. As shown in Fig. 3c, the linear fitting of slow-rate discharging data ($(\Delta t)^{1/2}$ in the range of 40 $s^{1/2}$ to 100 $s^{1/2}$, corresponding to discharge current density from 100 mA g^{-1} to 500 mA g^{-1}) and extrapolation to Δt=0 provided the capacitive specific energy of 239.1 mWh g^{-1} for TNO, 265.9 mWh g^{-1} for R-TNO, 287.9 mWh g^{-1} for MTNO and 304.1 mWh g^{-1} for R-MTNO. For R-MTNO, such capacitive specific energy contributes high percentages of 80.4 % at 100 mA g^{-1}, 85.7 % at 200 mA g^{-1}, and 90.7 % at 500 mA g^{-1}. For the other three materials, the capacitive contributions are slightly lower, yet still >65.6 % in the lowest case (TNO at 100 mA g^{-1}). Note such high capacitive contributions are achieved in micron-size coarse single crystals with extremely small specific surface area, which demonstrates D_{Li} in the lattice is sufficiently high to remove the diffusion limitations under 100-500 mA g^{-1}. Nevertheless, the specific energies begin to decrease and drop below the as-calculated capacitive ones at higher rates beyond 1,000 mA g^{-1} ($(\Delta t)^{1/2}$<40 $s^{1/2}$). Such observations are similarly found in super-capacitors, where the decline under extremely high rates could come from kinetic limitations, including electron transport at the electrode level, wetting of the liquid electrolyte, and ion transport in the liquid electrolyte. For our materials at the rates range considered, the latter two are unlikely to be the rate-limiting factors. This is because the composite electrodes of the four materials were prepared under the same conditions using the powders with similar size, morphology and specific surface area, thus having similar porosity and microstructure, yet R-MTNO does have much better rate performance than the reference sample TNO (Fig. 2b). Therefore, it again indicates the electron transport in the

composite electrodes to be the rate-controlling kinetic factor, which agrees with our previous analysis. This conclusion is consistent with our finding that electron doping by atmospheric hydrogen reduction helps to decrease the ohmic loss and improve the high-rate performance.

Lastly, to demonstrate the electrochemical performance of the synthesized R-MTNO in a more practical way, we assembled full cells paired with $LiNi_{0.5}Mn_{1.5}O_4$ cathode. After preparing the $LiNi_{0.5}Mn_{1.5}O_4$ cathode and the R-MTNO anode, we firstly investigated their electrochemical performance under different rates in separate half cells (using Li metal as the counter and reference electrode; charge-discharge curves plotted in Fig. 4a), in order to determine the areal loading/capacities of the cathode and anode and the voltage of the full cell (an optimal areal capacity ratio of cathode/anode = 1.13:1). Full-cell performances were next evaluated under current densities from 0.2 to 6.0 mA cm^{-2} (the specific capacity, as well as energy density, were based on the total mass of active materials in both electrodes). As shown in Fig. 4b and c, the full cells have relatively good rate performance up to 4.0 mA cm^{-2}, with a discharge capacity of 45.8 mAh g^{-1} (68.5 % retention with respect to the capacity at 0.2 mA cm^{-2}) at 4.0 mA cm^{-2}. The cycling capability at 2.0 mA cm^{-2} is also relatively stable for 500 cycles, with 0.1 % capacity loss per cycle, demonstrating the promising application as real-life batteries.

The coarse-grained R-TNO, MTNO and R-MTNO synthesized in the present work have several advantages. First of all, we compared our work and the representative literary/commercial Nb-based materials ($Ti_xNb_yO_{(4x+5y)/2}$, Nb_2O_5), Ti-based materials ($Li_4Ti_5O_{12}$ and TiO_2) and carbon materials (graphite) considering the particle size, specific surface area, electrode density, initial CE, volumetric energy density and volumetric power density [60, 61]. It is evident that increasing the particle size with uniform microstructure will result in smaller surface area (1.1 m^2 g^{-1} for R-MTNO, Fig. S10 and Table S5), higher electrode density (2.6 g cm^{-3} for R-MTNO**,** Fig. S11~12, and Table S6), and higher initial CE (99 % for R-MTNO, Table S7) as well as much more improved volumetric energy density (1338 Wh L^{-1} for R-MTNO) and volumetric power density (31200 W L^{-1} for R-MTNO, Fig. S13 and Table S7). Second, for the micro-sized materials with similar particle size (0.8~18 μm), the ones with higher theoretical densities (like 4.34 g cm^{-3} of $TiNb_2O_7$, 4.55 g cm^{-3} of Nb_2O_5) exhibit higher electrode densities compared with those with lower theoretical densities (like 3.41 g cm^{-3} of $Li_4Ti_5O_{12}$, 2.25 g cm^{-3} of graphite). Third, the micron-sized particles have a robust structure that does not crack upon cycling (see the microstructure of the cycled R-MTNO electrode in Fig. S14, which is essentially the same as the original one in Fig. S11). However, we do notice the formation of unknown phases at the surface of the R-MTNO particles, which could be solid electrolyte interphases (SEIs). Indeed, the gassing problem of TNO-based anode has been reported in the literature [62], which indicates the side reactions between the anode and the electrolyte. In this sense, the coarse-grained particles are also

advantageous in terms of smaller specific surface area and less side reactions. On the other hand, we believe the suspected SEI formation should be closely related to the huge overpotential under high rates and the capacity decay over long cycles. More detailed studies about SEIs should be investigated in this family of Nb-based oxide anodes and appropriate coating should be developed to improve the cycling performance. We have already shown that the electrode-level electron transport is the key factor that limits the high-rate performance of the investigated compounds. Therefore, carbon coating and modifications of the electrode structure to ensure better electron percolation would be possible methods for further improvement. Lastly, compared with recent reported $Ti_xNb_yO_{(4x+5y)/2}$ electrodes (Table S8), R-MTNO provides the most competitive cyclability considering the volumetric energy density at high rates; however, MTNO also shows improved high-rate performance than the reference sample TNO, which suggests MTNO could also be a good candidate material if the processing cost of the additional reduction treatment is a concern.

4. Conclusions

To summarize, a series of coarse-grained Mo substituted titanium niobium oxides were systematically studied with possible treatment in a reducing atmosphere and the optimal composition for high-rate applications as LIB anodes was found to be R-MTNO, $Mo_{0.25}Ti_{0.75}Nb_2O_{7.25-y}$. It can stably deliver a capacity of 208.0 mAh g^{-1} at 1,000 mA g^{-1} or ~5 C (83.8 % retention with respect to its capacity at 100 mA g^{-1}) and 158.5 mAh g^{-1} (65.2 % retention with respect to its capacity at 100 mA g^{-1}) at 6,000 mA g^{-1} (~40 C) vs. Li^+/Li, and show promising rate capability and cycling stability in full cells against $LiNi_{0.5}Mn_{1.5}O_4$ cathode. We found the main factor that limits the high-rate performance of TNO-related anodes is the huge overpotential developed under dynamic conditions, mostly from ohmic losses probably originating from the poor electronic percolation on the electrode level. Mo substitution and reduction treatment are simple and effective methods to solve this kinetic problem, and further modifications by coating and optimizing the electrode structure are expected to work synergistically to boost the high-rate performance. More generally, we recommend diagnosis using GITT analysis to better understand the kinetic problems at the electrode level, so that specific modification strategies could be applied accordingly.

Acknowledgements

L.Z. and S.W. contributed equally to this work. J. Z. acknowledges the support of the State Key Laboratory of New Ceramic and Fine Processing Tsinghua University (No. KF201801). Z.T. acknowledges support by the National Natural Science Foundation of China (No. 51772163). J.L. acknowledges support by Wuxi Weifu High-Technology Group Co., Ltd.

Declaration of competing interest

The authors declare that they have no known competing financial interests or personal relationships that could have appeared to influence the work reported in this paper.

Appendix A. Supplementary data

Supplementary data to this article can be found online at.

References

[1] Y. Liu, Y. Zhu, Y. Cui, Challenges and opportunities towards fast-charging battery materials, Nature Energy 4 (2019) 540-550.

[2] S. Wang, Z. Zhang, Y. Yang, Z. Tang, Efficient Lithium-Ion Storage by Hierarchical Core-Shell TiO_2 Nanowires Decorated with MoO_2 Quantum Dots Encapsulated in Carbon Nanosheets, ACS Appl. Mater. Interfaces 9 (2017) 23741-23747.

[3] S. Wang, F. Cao, Y. Li, Z. Zhang, D. Zhou, Y. Yang, Z. Tang, MoS_2-Coupled Carbon Nanosheets Encapsulated on Sodium Titanate Nanowires as Super-Durable Anode Material for Sodium-Ion Batteries, Adv. Sci. (2019) 1900028.

[4] S. Wang, Y. Yang, Y. Dong, Z. Zhang, Z. Tang, Recent progress in Ti-based nanocomposite anodes for lithium ion batteries, J. Adv. Ceram. 8 (2019) 1-18.

[5] S. Wang, Y. Yang, C. Jiang, Y. Hong, W. Quan, Z. Zhang, Z. Tang, Nitrogen-doped carbon coated $Li_4Ti_5O_{12}$-TiO_2/Sn nanowires and their enhanced electrochemical properties for lithium ion batteries, J. Mater. Chem. A 4 (2016) 12714-12719.

[6] Y. Yang, S. Wang, M. Luo, W. Wang, F. Lv, Z. Tang, S. Guo, $Li_4Ti_5O_{12}$-TiO_2/MoO_2 nanoclusters-embedded into carbon nanosheets core/shell porous superstructures boost lithium ion storage, J. Mater. Chem. A 5 (2017) 12096-12102.

[7] L. Zhao, S. Wang, F. Pan, Z. Tang, Z. Zhang, S. Zhong, J. Zhang, Thermal convection induced TiO_2 microclews as superior electrode materials for lithium-ion batteries, J. Mater. Chem. A 6 (2018) 11688-11693.

[8] S. Wang, Y. Yang, W. Quan, Y. Hong, Z. Zhang, Z. Tang, J. Li, Ti^{3+}-free three-phase $Li_4Ti_5O_{12}$/TiO_2 for high-rate lithium ion batteries: Capacity and conductivity enhancement by phase boundaries, Nano Energy 32 (2017) 294-301.

[9] S. Wang, W. Quan, Z. Zhu, Y. Yang, Q. Liu, Y. Ren, X. Zhang, R. Xu, Y. Hong, Z. Zhang, K. Amine, Z. Tang, J. Lu, J. Li, Lithium titanate hydrates with superfast and stable cycling in lithium ion batteries, Nat. Commun. 8 (2017) 627.

[10] X. Liu, L. Zhao, S. Wang, M. Chao, Y. Li, J. Leng, J. Zhang, Z. Tang, Hierarchical-structure anatase TiO_2 with conductive network for high-rate and high-loading lithium-ion battery, Sci Bull 64 (2019) 1148-1151.

[11] Y. Yang, S. Wang, S. Lin, Y. Li, W. Zhang, Y. Chao, M. Luo, Y. Xing, K. Wang, C. Yang, P. Zhou, Y. Zhang, Z. Tang, S. Guo, Rational Design of Hierarchical TiO_2/Epitaxially Aligned MoS_2-Carbon Coupled Interface Nanosheets Core/Shell Architecture for Ultrastable Sodium-Ion and Lithium-Sulfur Batteries, Small Methods (2018) 1800119.

[12] T. Yuan, Z. Tan, C. Ma, J. Yang, Z.-F. Ma, S. Zheng, Challenges of Spinel $Li_4Ti_5O_{12}$ for Lithium-Ion Battery Industrial Applications, Adv. Energy Mater. 7 (2017) 1601625.

[13] Z. Liu, W. Dong, J. Wang, C. Dong, Y. Lin, I.W. Chen, F. Huang, Orthorhombic Nb_2O_{5-x} for Durable High-Rate Anode of Li-Ion Batteries, iScience 23 (2020) 100767.

[14] K.J. Griffith, A.C. Forse, J.M. Griffin, C.P. Grey, High-Rate Intercalation without Nanostructuring in Metastable Nb_2O_5 Bronze Phases, J. Am. Chem. Soc. 138 (2016) 8888-8899.

[15] J.F. Colin, V. Pralong, M. Hervieu, V. Caignaert, B. Raveau, Lithium insertion in an oriented nanoporous oxide with a tunnel structure: $Ti_2Nb_2O_9$, Chem. Mater. 20 (2008) 1534-1540.

[16] J.T. Han, Y.H. Huang, J.B. Goodenough, New Anode Framework for Rechargeable Lithium Batteries, Chem. Mater. 23 (2011) 2027-2029.

[17] X. Lu, Z. Jian, Z. Fang, L. Gu, Y.-S. Hu, W. Chen, Z. Wang, L. Chen, Atomic-scale investigation on lithium storage mechanism in $TiNb_2O_7$, Energy Environ. Sci. 4 (2011) 2638-2644.

[18] K.J. Griffith, K.M. Wiaderek, G. Cibin, L.E. Marbella, C.P. Grey, Niobium tungsten oxides for high-rate lithium-ion energy storage, Nature 559 (2018) 556-563.

[19] J.-T. Han, J.B. Goodenough, 3-V Full Cell Performance of Anode Framework $TiNb_2O_7$/Spinel $LiNi_{0.5}Mn_{1.5}O_4$, Chem. Mater. 23 (2011) 3404-3407.

[20] N. Takami, K. Ise, Y. Harada, T. Iwasaki, T. Kishi, K. Hoshina, High-energy, fast-charging, long-life lithium-ion batteries using $TiNb_2O_7$ anodes for automotive applications, J. Power Sources 396 (2018) 429-436.

[21] L. Hu, L. Luo, L. Tang, C. Lin, R. Li, Y. Chen, $Ti_2Nb_{2x}O_{4+5x}$ anode materials for lithium-ion batteries: a comprehensive review, J. Mater. Chem. A 6 (2018) 9799-9815.

[22] Q. Deng, Y. Fu, C. Zhu, Y. Yu, Niobium-Based Oxides Toward Advanced Electrochemical Energy Storage: Recent Advances and Challenges, Small 15 (2019) e1804884.

[23] L. Shen, Y. Wang, H. Lv, S. Chen, P.A. van Aken, X. Wu, J. Maier, Y. Yu, Ultrathin $Ti_2Nb_2O_9$ Nanosheets with Pseudocapacitive Properties as Superior Anode for Sodium-Ion Batteries, Adv. Mater. (2018) 1804378.
[24] H. Park, H.B. Wu, T. Song, X.W. David Lou, U. Paik, Porosity-Controlled $TiNb_2O_7$ Microspheres with Partial Nitridation as A Practical Negative Electrode for High-Power Lithium-Ion Batteries, Adv. Energy Mater. 5 (2015) 1401945.
[25] K. Tang, X. Mu, P.A. van Aken, Y. Yu, J. Maier, "Nano-Pearl-String" $TiNb_2O_7$ as Anodes for Rechargeable Lithium Batteries, Adv. Energy Mater. 3 (2013) 49-53.
[26] B. Guo, X. Yu, X.-G. Sun, M. Chi, Z.-A. Qiao, J. Liu, Y.-S. Hu, X.-Q. Yang, J.B. Goodenough, S. Dai, A long-life lithium-ion battery with a highly porous $TiNb_2O_7$ anode for large-scale electrical energy storage, Energy Environ. Sci. 7 (2014) 2220-2226.
[27] S. Lou, X. Cheng, Y. Zhao, A. Lushington, J. Gao, Q. Li, P. Zuo, B. Wang, Y. Gao, Y. Ma, C. Du, G. Yin, X. Sun, Superior performance of ordered macroporous $TiNb_2O_7$ anodes for lithium ion batteries: Understanding from the structural and pseudocapacitive insights on achieving high rate capability, Nano Energy 34 (2017) 15-25.
[28] X. Wang, G. Shen, Intercalation pseudo-capacitive $TiNb_2O_7$@carbon electrode for high-performance lithium ion hybrid electrochemical supercapacitors with ultrahigh energy density, Nano Energy 15 (2015) 104-115.
[29] H. Yu, H. Lan, L. Yan, S. Qian, X. Cheng, H. Zhu, N. Long, M. Shui, J. Shu, $TiNb_2O_7$ hollow nanofiber anode with superior electrochemical performance in rechargeable lithium ion batteries, Nano Energy 38 (2017) 109-117.
[30] H. Song, Y.T. Kim, A Mo-doped $TiNb_2O_7$ anode for lithium-ion batteries with high rate capability due to charge redistribution, Chem Commun (Camb) 51 (2015) 9849-9852.
[31] X. Wen, C. Ma, C. Du, J. Liu, X. Zhang, D. Qu, Z. Tang, Enhanced electrochemical properties of vanadium-doped titanium niobate as a new anode material for lithium-ion batteries, Electrochim. Acta 186 (2015) 58-63.
[32] C. Yang, C. Lin, S. Lin, Y. Chen, J. Li, $Cu_{0.02}Ti_{0.94}Nb_{2.04}O_7$: An advanced anode material for lithium-ion batteries of electric vehicles, J. Power Sources 328 (2016) 336-344.
[33] C. Lin, S. Yu, H. Zhao, S. Wu, G. Wang, L. Yu, Y. Li, Z.Z. Zhu, J. Li, S. Lin, Defective $Ti_2Nb_{10}O_{27}$.1: an advanced anode material for lithium-ion batteries, Sci Rep 5 (2015) 17836.
[34] T. Takashima, T. Tojo, R. Inada, Y. Sakurai, Characterization of mixed titanium–niobium oxide $Ti_2Nb_{10}O_{29}$ annealed in vacuum as anode material for lithium-ion battery, J. Power Sources 276 (2015) 113-119.

[35] C. Pham, J.H. Choi, J. Yun, A.S. Bandarenka, J. Kim, P.V. Braun, S.Y. Jeong, C.R. Cho, Synergistically Enhanced Electrochemical Performance of Hierarchical $MoS_2/TiNb_2O_7$ Hetero-nanostructures as Anode Materials for Li-Ion Batteries, ACS Nano 11 (2017) 1026-1033.
[36] C. Lin, L. Hu, C. Cheng, K. Sun, X. Guo, Q. Shao, J. Li, N. Wang, Z. Guo, Nano-$TiNb_2O_7$/carbon nanotubes composite anode for enhanced lithium-ion storage, Electrochim. Acta 260 (2018) 65-72.
[37] S. Li, X. Cao, C.N. Schmidt, Q. Xu, E. Uchaker, Y. Pei, G. Cao, $TiNb_2O_7$/graphene composites as high-rate anode materials for lithium/sodium ion batteries, J. Mater. Chem. A 4 (2016) 4242-4251.
[38] H. Li, L. Shen, J. Wang, S. Fang, Y. Zhang, H. Dou, X. Zhang, Three-dimensionally ordered porous $TiNb_2O_7$ nanotubes: a superior anode material for next generation hybrid supercapacitors, J. Mater. Chem. A 3 (2015) 16785-16790.
[39] H. Park, D.H. Shin, T. Song, W.I. Park, U. Paik, Synthesis of hierarchical porous $TiNb_2O_7$ nanotubes with controllable porosity and their application in high power Li-ion batteries, J. Mater. Chem. A 5 (2017) 6958-6965.
[40] H. Park, T. Song, U. Paik, Porous $TiNb_2O_7$ nanofibers decorated with conductive $Ti_{1-x}Nb_xN$ bumps as a high power anode material for Li-ion batteries, J. Mater. Chem. A 3 (2015) 8590-8596.
[41] H. Li, L. Shen, G. Pang, S. Fang, H. Luo, K. Yang, X. Zhang, $TiNb_2O_7$ nanoparticles assembled into hierarchical microspheres as high-rate capability and long-cycle-life anode materials for lithium ion batteries, Nanoscale 7 (2015) 619-624.
[42] Q. Cheng, J. Liang, N. Lin, C. Guo, Y. Zhu, Y. Qian, Porous $TiNb_2O_7$ Nanospheres as ultra Long-life and High-power Anodes for Lithium-ion Batteries, Electrochim. Acta 176 (2015) 456-462.
[43] C. Jo, Y. Kim, J. Hwang, J. Shim, J. Chun, J. Lee, Block Copolymer Directed Ordered Mesostructured $TiNb_2O_7$ Multimetallic Oxide Constructed of Nanocrystals as High Power Li-Ion Battery Anodes, Chem. Mater. 26 (2014) 3508-3514.
[44] M. Park, X. Zhang, M. Chung, G.B. Less, A.M. Sastry, A review of conduction phenomena in Li-ion batteries, J. Power Sources 195 (2010) 7904-7929.
[45] S. Andersson, A. Wadsley, Crystallographic shear and diffusion paths in certain higher oxides of niobium, tungsten, molybdenum and titanium, Nature 211 (1966) 581-583.
[46] L. Perfler, V. Kahlenberg, C. Wikete, D. Schmidmair, M. Tribus, R. Kaindl, Nanoindentation, High-Temperature Behavior, and Crystallographic/Spectroscopic Characterization of the High-Refractive-Index Materials $TiTa_2O_7$ and $TiNb_2O_7$, Inorg. Chem. 54 (2015) 6836-6848.
[47] Z. Wang, C. Yang, T. Lin, H. Yin, P. Chen, D. Wan, F. Xu, F. Huang, J. Lin, X. Xie, M. Jiang, Visible-light photocatalytic, solar thermal and photoelectrochemical properties of aluminium-reduced black titania, Energy Environ. Sci. 6 (2013) 3007-2014.

[48] Y. Dong, I.W. Chen, Electrical and hydrogen reduction enhances kinetics in doped zirconia and ceria:II. Mapping electrode polarization and vacancy condensation inYSZ, J. Am. Ceram. Soc. 101 (2017) 1058-1073.
[49] Y. Dong, H. Wang, I.W. Chen, Electrical and hydrogen reduction enhances kinetics in doped zirconia and ceria: I. grain growth study, J. Am. Ceram. Soc. 100 (2017) 876-886.
[50] J. Qiu, C. Lai, E. Gray, S. Li, S. Qiu, E. Strounina, C. Sun, H. Zhao, S. Zhang, Blue hydrogenated lithium titanate as a high-rate anode material for lithium-ion batteries, J. Mater. Chem. A 2 (2014) 6353-6358.
[51] C. Wang, W. Chen, D. Yuan, S. Qian, D. Cai, J. Jiang, S. Zhang, Tailoring the nanostructure and electronic configuration of metal phosphides for efficient electrocatalytic oxygen evolution reactions, Nano Energy 69 (2020) 104453.
[52] J. Qiu, S. Li, E. Gray, H. Liu, Q.-F. Gu, C. Sun, C. Lai, H. Zhao, S. Zhang, Hydrogenation Synthesis of Blue TiO_2 for High-Performance Lithium-Ion Batteries, J. Phys. Chem. C 118 (2014) 8824-8830.
[53] P.A. Spevack, N.S. McIntyre, A Raman and XPS investigation of supported molybdenum oxide thin films. 1. Calcination and reduction studies, J. Phys. Chem. 97 (1993) 11020-11030.
[54] S.Y. Lee, N. Mettlach, N. Nguyen, Y.M. Sun, J.M. White, Copper oxide reduction through vacuum annealing, Appl. Surf. Sci. 206 (2003) 102-109.
[55] S. Poulston, P. Parlett, P. Stone, M. Bowker, Surface oxidation and reduction of CuO and Cu_2O studied using XPS and XAES, Surf. Interface Anal. 24 (1996) 811-820.
[56] W. Weppner, Determination of the Kinetic Parameters of Mixed-Conducting Electrodes and Application to the System Li_3Sb, J. Electrochem. Soc. 124 (1977) 1569-1578.
[57] Y. Li, S. Wang, Y. Dong, Y. Yang, Z. Zhang, Z. Tang, Glass‐Ceramic‐Like Vanadate Cathodes for High‐Rate Lithium‐Ion Batteries, Adv. Energy Mater. 10 (2019) 1903411.
[58] T. Lin, I.W. Chen, F. Liu, C. Yang, H. Bi, F. Xu, F. Huang, Nitrogen-doped mesoporous carbon of extraordinary capacitance for electrochemical energy storage, Science 350 (2015) 1508-1513.
[59] V. Augustyn, J. Come, M.A. Lowe, J.W. Kim, P.L. Taberna, S.H. Tolbert, H.D. Abruna, P. Simon, B. Dunn, High-rate electrochemical energy storage through Li^+ intercalation pseudocapacitance, Nat. Mater. 12 (2013) 518-522.
[60] Z. Fan, C. Wei, L. Yu, Z. Xia, J. Cai, Z. Tian, G. Zou, S.X. Dou, J. Sun, 3D Printing of Porous Nitrogen-Doped Ti_3C_2 MXene Scaffolds for High-Performance Sodium-Ion Hybrid Capacitors, ACS Nano 14 (2020) 867-876.

[61] C. Li, S. Cong, Z. Tian, Y. Song, L. Yu, C. Lu, Y. Shao, J. Li, G. Zou, M.H. Rümmeli, S. Dou, J. Sun, Z. Liu, Flexible perovskite solar cell-driven photo-rechargeable lithium-ion capacitor for self-powered wearable strain sensors, Nano Energy 60 (2019) 247-256.
[62] X. Wu, S. Lou, X. Cheng, C. Lin, J. Gao, Y. Ma, P. Zuo, C. Du, Y. Gao, G. Yin, Unravelling the Interface Layer Formation and Gas Evolution/Suppression on a $TiNb_2O_7$ Anode for Lithium-Ion Batteries, ACS Appl Mater Interfaces 10 (2018) 27056-27062.

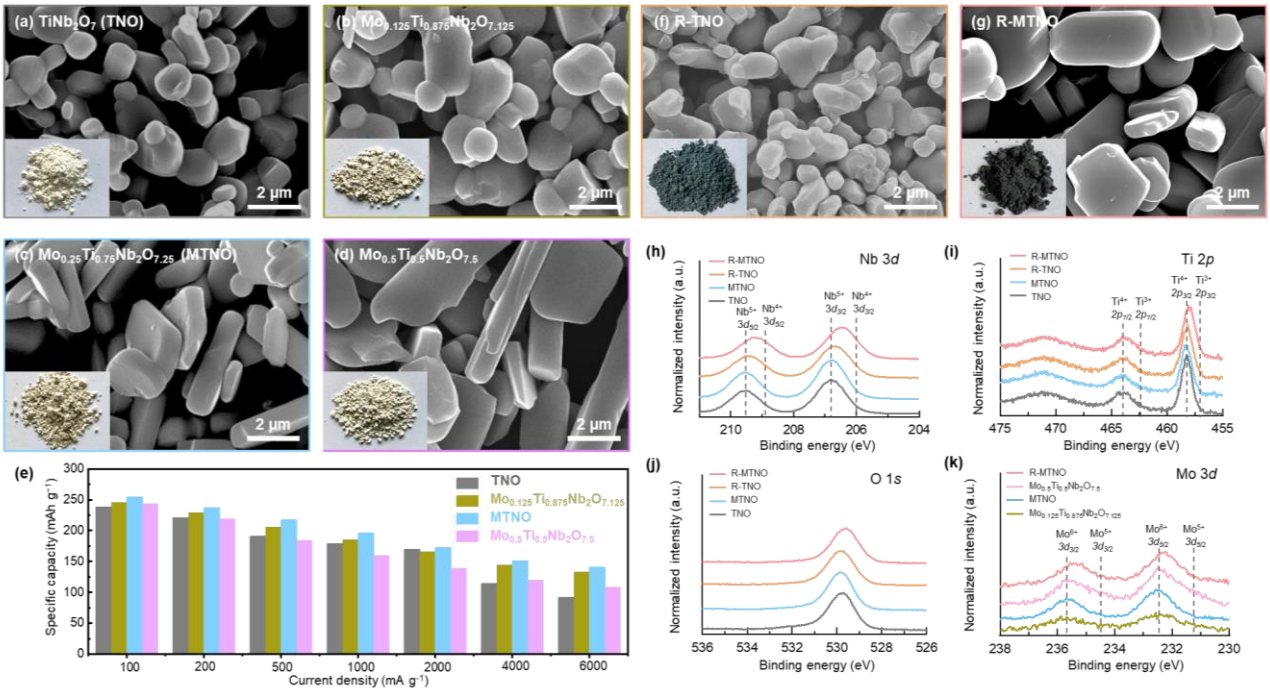

Fig. 1. Microstructure of (a) $TiNb_2O_7$ (TNO), (b) $Mo_{0.125}Ti_{0.875}Nb_2O_{7.125}$, (c) $Mo_{0.25}Ti_{0.75}Nb_2O_{7.25}$ (MTNO), (d) $Mo_{0.5}Ti_{0.5}Nb_2O_{7.5}$, (f) reduced TNO (R-TNO), and (g) reduced MTNO (R-MTNO). (e) Specific capacities of (a-d) under different rates. XPS spectra of (h) Nb 3*d*, (i) Ti 2*p*, (j) O 1*s*, (k) Mo 3*d* for TNO, MTNO, R-TNO and R-MTNO. Insets of (a-d), (f-g): photos of corresponding materials.

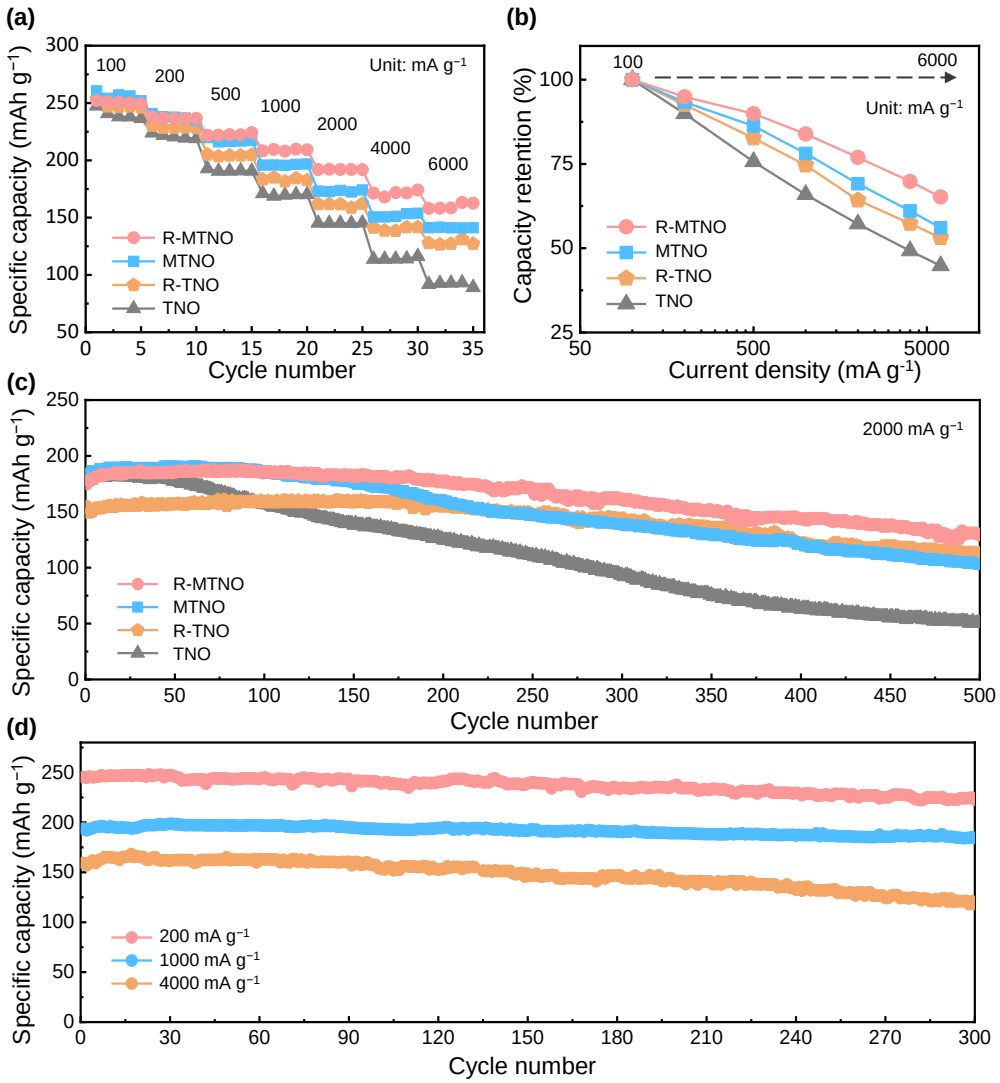

Fig. 2. (a) Rate performance, (b) capacity retention under different rates, (c) cycling performance of R-MTNO, MTNO, R-TNO and TNO at 2000 mA g^{-1}. (d) Cycling performance of R-MTNO at 200, 1000 and 4000 mA g^{-1}.

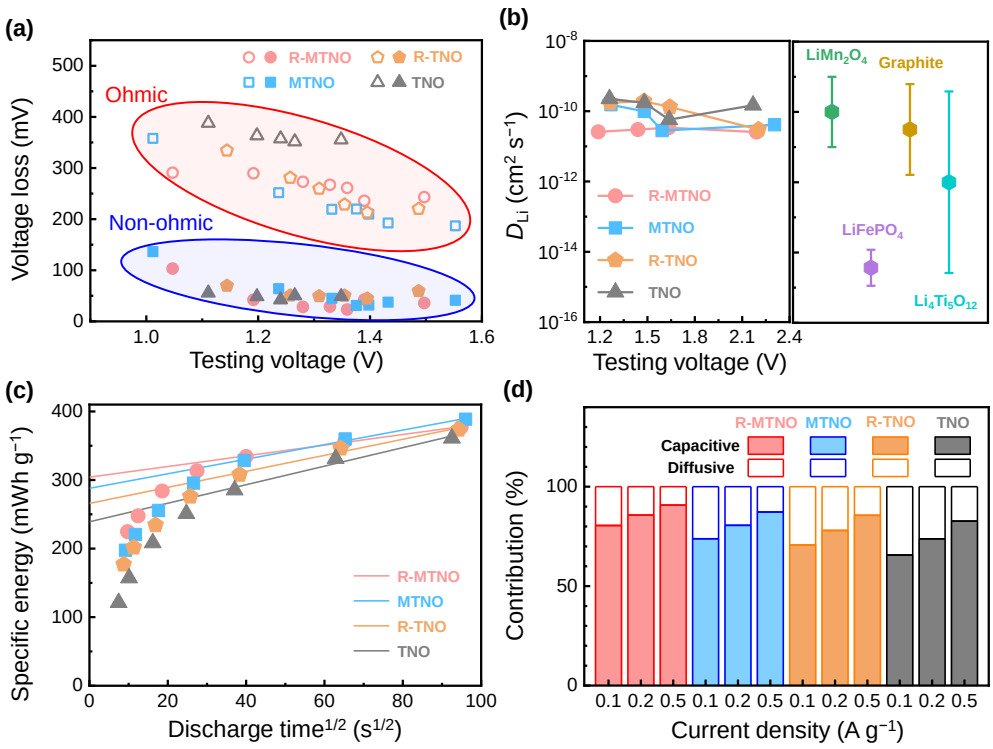

Fig. 3. (a) Ohmic and non-ohmic losses of R-MTNO, MTNO, R-TNO and TNO at different testing voltages. (b) Calculated diffusion coefficients of R-MTNO, MTNO, R-TNO and TNO, together with comparison with literature values for $LiMn_2O_4$, $LiFePO_4$, graphite and $Li_4Ti_5O_{12}$. (c) Specific energy vs. square root of half-cycle time and (d) calculated contributions from capacitive and diffusive charge storage for R-MTNO, MTNO, R-TNO and TNO.

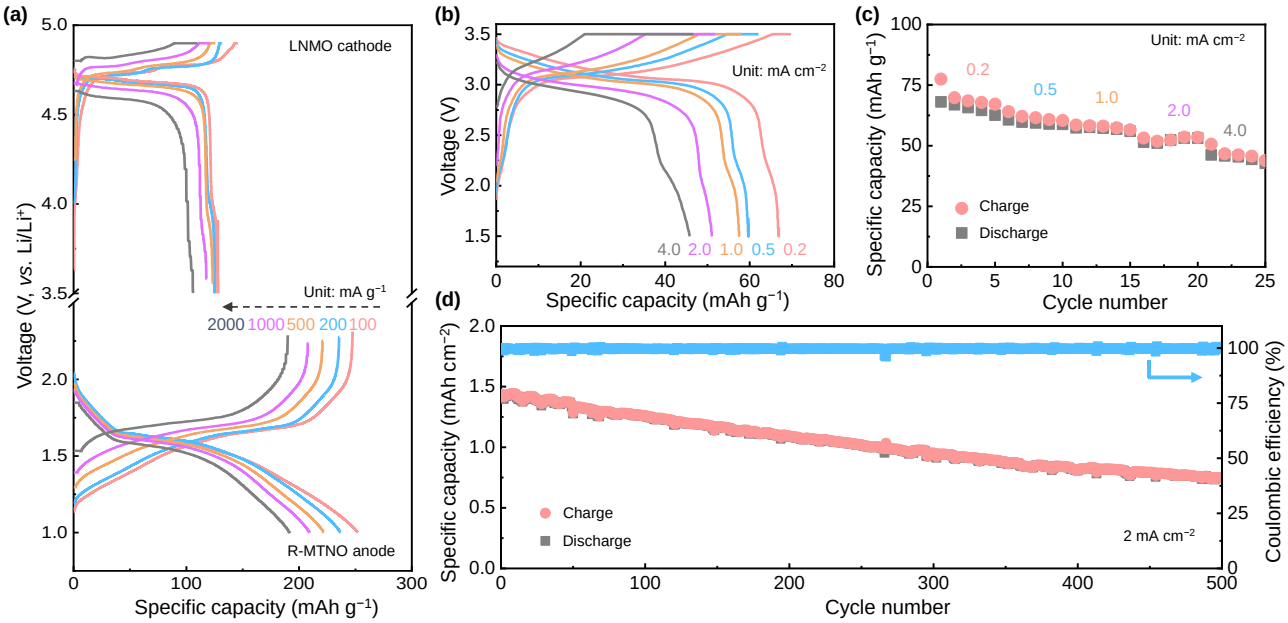

Fig. 4. (a) Galvanostatic discharge/charge profiles for $LiNi_{0.5}Mn_{1.5}O_4$ cathode and R-MTNO anode. (b) Galvanostatic discharge/charge profiles, (c) rate performance and (d) cycling performance of $LiNi_{0.5}Mn_{1.5}O_4$ || R-MTNO full cells.